

# Optimization of Dielectric-Metal Multilayer Structure for Color-Preserving Radiative Cooling Window

Guowei Liu, Shujing Chen,\* and Chengyou Lin\*

Cite This: *ACS Omega* 2024, 9, 30425–30435

Read Online

ACCESS |



Metrics &amp; More

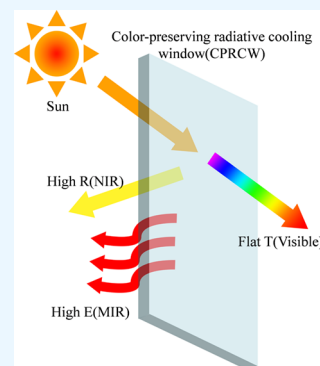


Article Recommendations



Supporting Information

**ABSTRACT:** Radiative cooling window has been designed to emit infrared radiation in the atmospheric transparency window and reflects near-infrared light while allowing visible light to pass through. However, improvements are still needed in the transmissivity of visible light, the reflectivity of near-infrared light, and emissivity of mid-infrared spectra. This paper proposes a color-preserving radiative cooling window consisting of a multilayer film as a transparent near-infrared reflector and polydimethylsiloxane (PDMS) as a thermal emitter. This design involves optimizing the types of film materials, the number of layers, and the thicknesses of the films through a genetic algorithm. The performance of multilayer films with various layer numbers is compared, and we choose 7-layer multilayer film ( $\text{Al}_2\text{O}_3/\text{Ag}/\text{Al}_2\text{O}_3/\text{Ag}/\text{Al}_2\text{O}_3/\text{Ag}/\text{Al}_2\text{O}_3$ ) as the transparent near-infrared reflector. Then, we analyze its spectral characteristics in depth. Sequentially, we place a 100- $\mu\text{m}$ -thick PDMS as a thermal emitter above the transparent near-infrared reflector. By combining the transparent near-infrared reflector with the PDMS and utilizing genetic algorithm, a color-preserving radiative cooling window has been achieved with flat and broadband average visible transmittance (86%), high average near-infrared reflectance (86%), high average thermal emissivity (95%) in the atmospheric window, and the drop of temperature (22.3, 21.2, and 15.8 K when nonradiative heat coefficient is, respectively, 0, 6, and 12  $\text{W}/\text{m}^2/\text{K}$ ).



## 1. INTRODUCTION

Nowadays, over 30% of the total energy consumption is attributed to heating, cooling, ventilation, and artificial lighting for buildings.<sup>1,2</sup> Windows are a crucial factor in a building's energy consumption due to the substantial amount of light and heat that passes through windows. A common approach to energy-saving windows<sup>3</sup> is to use an infrared filter on standard glass, blocking sunlight in the infrared band while allowing light in the visible band to pass through, thus lowering indoor temperatures.<sup>4</sup> Several types of energy-saving windows have attracted much attention, such as transparent heat reflectors, electrochromic windows, and thermochromic windows. For instance, in 2016, Dalapati et al. proposed a  $\text{TiO}_2/\text{Cu}/\text{TiO}_2$  multilayer thin film on glass that can serve as a heat reflector, providing the highest transmittance of 90% at visible wavelength and an IR reflectance of 85% at a wavelength of 1200 nm.<sup>5</sup> In 2018, Piccolo et al. described the results of experimental tests and computer simulation modeling aimed at evaluating the performance of an electrochromic (EC) window, providing evidence that the investigated EC device is effective in reducing heat loads.<sup>6</sup> In 2019, Salamati et al. proposed a new type thermochromic coatings to reflect unwanted near-infrared radiation in summer, offering additional energy savings.<sup>7</sup> Despite these innovations, traditional infrared filters for energy-saving windows still contribute to an increase in indoor temperatures because of passing through most of the visible light, which indicates the need for new strategies in energy-saving window designs to enhance cooling efficiency further.

Radiative cooling offers a method for passive temperature regulation. It primarily produces high emission within the 8–13  $\mu\text{m}$  atmospheric window, allowing heat to be radiated directly into the outer space while reflecting all solar radiation (0.3–2.5  $\mu\text{m}$ ) to minimize heat load.<sup>8</sup> This approach is increasingly recognized for its potential to cut energy use, reduce  $\text{CO}_2$  emissions, and mitigate the greenhouse effect.<sup>3,9–12</sup> For effective radiative cooling, a device should exhibit high emissivity in the atmospheric window (8–13  $\mu\text{m}$ ) and high reflectivity within the solar radiation range.<sup>13,14</sup> When the cooler exhibits high transmittance within the visible light spectrum, high reflectance in the NIR band, and high emittance through the atmospheric window, it qualifies as a transparent radiative cooler. For example, in 2023, Guan et al.<sup>15</sup> theoretically designed and optimized a transmissive colored radiative cooling film that allows a specific portion of light to pass through and provides more vivid colors by means of a mixed-integer memetic algorithm and machine learning. In 2024, Li et al.<sup>16</sup> theoretically proposed an adaptive radiative cooling system based on  $\text{W}-\text{VO}_2$ , where the spectra at high and low temperatures can be

Received: February 24, 2024

Revised: May 17, 2024

Accepted: June 20, 2024

Published: July 2, 2024



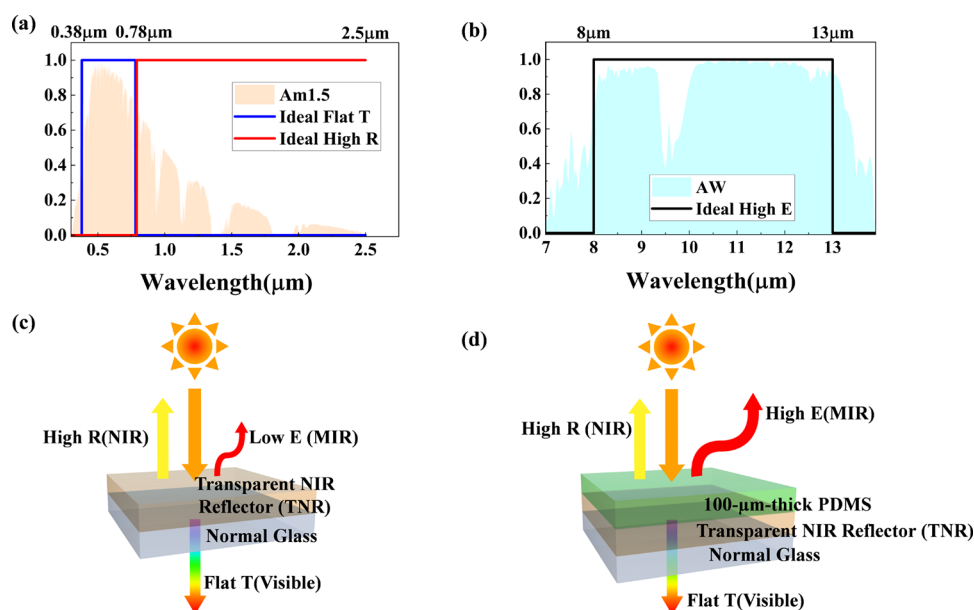


**Figure 1.** (a) Reflectance and transmittance spectra and (b) emissivity spectrum of the ideal transparent radiative window. (c) Schematic illustration of a transparent NIR reflector. (d) Schematic illustration of a color-preserving radiative cooling window.

easily adjusted by varying the thickness of each layer and the ratio of  $W\text{-VO}_2$ . Currently, such cooling techniques are employed in solar cells,<sup>17</sup> thermoelectric generator cooling,<sup>18</sup> triboelectric nanogenerator,<sup>19–21</sup> thermoelectric power generator,<sup>22</sup> radiative coolers that modulate color,<sup>11,15,23,24</sup> transparent radiative cooling window,<sup>9,25,26</sup> and so on.

When energy-saving windows are combined with radiative cooling, the concept of radiative cooling window has emerged. Apart from maintaining high reflectivity in the near-infrared (NIR, 0.78–2.5  $\mu\text{m}$ ) band and high emissivity in the atmospheric window (AW, 8–13  $\mu\text{m}$ ), these windows should also have high transmissivity in the visible band (VIS, 0.38–0.78  $\mu\text{m}$ ) to ensure both transparency and cooling.<sup>27–32</sup> Currently, various multilayer thin-film designs for radiative cooling windows are under exploration. For instance, in 2021, Kim et al.<sup>25</sup> proposed a dielectric multilayer consisting of hydrogenated amorphous silicon (a-Si:H) and  $\text{SiO}_2$  stacked alternatively and a top polydimethylsiloxane (PDMS) layer on a glass, which reduced the temperature by up to 14.4 K. In 2022, a dielectric/metal/dielectric (DMD) transparent radiative cooling structure ( $\text{ZnO}/\text{Ag}/\text{ZnO}$ ) with 77% visible light transmissivity, 57% NIR reflectivity, and 91% atmospheric window emissivity was proposed by Dang et al.<sup>33</sup> Zhang et al. proposed a radiative cooling glass with a PDMS/ITO/ $\text{SiO}_2$  structure that can achieve a visible light transmissivity of 80.5%, NIR reflectivity of 10.3%, and atmospheric window emissivity of 94.8%.<sup>26</sup> Jin et al. achieves wavelength selectivity through a 1D planar hyperbolic metamaterial (HMMs) design to realize near an epsilon-near-zero (ENZ) region, utilizing a structure of hyperbolic materials with a periodic multilayer film configuration (three pairs of  $\text{SiO}_2$  115 nm/Ag 12 nm and an additional top layer of  $\text{SiO}_2$  60 nm). After combining the HMM with the PDMS, it results in high visible transparency (>60%), IR reflectivity (>89%), and thermal emissivity (>95%)<sup>24</sup>

Many research studies have been done in the field of transparent radiative cooling. However, currently, there are few works addressing color-preserving.<sup>34,35</sup> In this work, we utilize the mixed-integer genetic algorithm<sup>36,37</sup> (GA) and the transfer matrix method<sup>38–39</sup> (TMM) to optimize an aperiodic multilayer

structure as a transparent NIR reflector (TNR), which features flat visible transmittance for color-preserving and high reflectance in the NIR band. By taking full advantage of the mixed-integer GA and TMM, the layer materials types, the number of layers, and thicknesses of the TNR have been simultaneously optimized. The optimization process of the GA finally converged to dielectric-metal multilayer structures, which are taken as the TNR. Sequentially, we place a 100- $\mu\text{m}$ -thick polydimethylsiloxane (PDMS) as a thermal emitter above the TNR to enhance the emission in the atmospheric window. By combining the TNR with a 100- $\mu\text{m}$ -thick PDMS, a color-preserving radiative cooling window (CPRCW) has been achieved by the GA, with flat and broadband average visible transmittance (86%) for color-preserving and visibility, high average near-infrared reflectance (86%) for blocking incoming NIR solar radiation, high average thermal emissivity (95%) in the atmospheric window for releasing heat into the outer space, and the drop of temperature (22.3, 21.2, and 15.8 K when nonradiative heat coefficient is, respectively, 0, 6, and 12  $\text{W}/\text{m}^2/\text{K}$ ). We further analyze the spectral characteristics and cooling performance of the proposed CPRCW.

## 2. THEORY

### 2.1. Color-Preserving Radiative Cooling Window Structure.

The CPRCW proposed in this article encompasses multispectral manipulation in the VIS, NIR, and MIR areas. As depicted in Figure 1a,b, an ideal CPRCW should satisfy a flat transmittance curve in the visible band, a reflectance of 1 in the near-infrared band, and an emittance of 1 in the atmospheric window. Given that these multispectral characteristics are closely coupled, minor modifications in structure or material composition can influence transmissivity, reflectance, and emissivity, impacting cooling efficiency and visibility.<sup>15</sup> Thus, designing multilayer films to simultaneously achieve high visible transmittance, high near-infrared reflectance, and high middle-infrared emittance is challenging due to these factors. As a solution, we first design a TNR whose transmissivity is uniformly flat, to preserve the color of incident sunlight. Besides, the

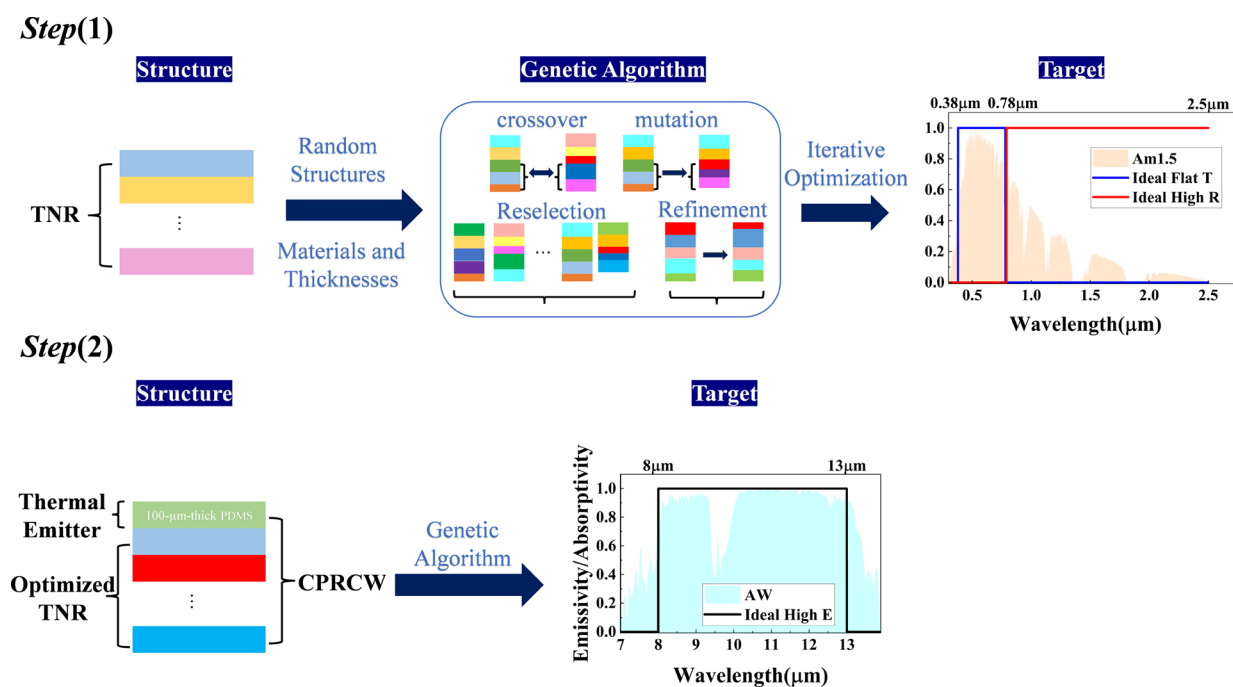


**Figure 2.** Step(1): The proposed transparent NIR reflector starts with genetic optimization of a multilayer film, whose layer materials, thicknesses, and number of layers are simultaneously optimized to pursue the desired multispectral characteristics. Step(2): The optimized TNR is then combined with a thermal emitter to enhance the emission within the atmospheric window.

average NIR reflectivity of the TNR is extremely high to stop the incident NIR solar radiation (Figure 1c). However, the TNR which shows a low middle-infrared emittance (8–13 μm) cannot have enough cooling performance. Second, we place a 100-μm-thick PDMS as a thermal emitter above the TNR to enhance the emissivity in the middle-infrared band (see Figure 1d). The PDMS layer, when uniformly spread over the TNR structure, serves as an efficient thermal emitter due to its pronounced thermal emission at mid-IR wavelengths beyond 3 μm.<sup>24</sup> This configuration cleverly separates the color-preserving TNR and the thermal emitter, as shown in Figure 1d: (i) the lower TNR has uniformly flat transmittance in visible wavelength, blocking incoming NIR solar radiation; (ii) the upper PDMS serves as the thermal emitter, continuously releasing heat into space through atmospheric windows for radiative cooling. In the field of radiative cooling, there are many other papers that have also employed this method.<sup>15,24,35</sup> By combination of TNR with the thermal emitter (PDMS), the concept of radiative cooling windows has emerged. Due to the minimal impact on each other, the designs for the lower TNR and the upper emitter can be optimized one after the other. To calculate the radiative cooling performance of the proposed radiative cooling window, the cooling power  $P_{\text{cool}}$  per unit area at temperature  $T$  is expressed by  $P_{\text{cool}}(T)$ . The radiative cooler is affected by the influence of both solar irradiance and atmospheric thermal radiation (corresponding to the ambient air temperature  $T_{\text{amb}}$ ) when exposed to the daytime sky.<sup>14</sup> The related formula of radiative cooling is recorded in Supporting Information S11.

**2.2. The Refractive Index of Materials.** Here, in order to realize the original design intention of achieving the spectral selectivity by combining different electromagnetic responses, we take silver (Ag), silicon dioxide ( $\text{SiO}_2$ ), aluminum oxide ( $\text{Al}_2\text{O}_3$ ), titanium dioxide ( $\text{TiO}_2$ ), and magnesium fluoride ( $\text{MgF}_2$ ),<sup>40–43</sup> as the candidate materials for the multilayer structure, which are compatible with thin-film fabrication.

Besides, the PDMS<sup>44,45</sup> is taken as the thermal emitter. The detailed refractive index of the above materials can be seen in Supporting Information S12. The choice of these specific candidate dielectric materials is based on multiple factors. First, they are used for passive radiative cooling.<sup>24,26,46,47</sup> Second, they exhibit a near-zero extinction coefficient in the visible and NIR regimes, which means low absorption and is beneficial for transmitting light from a window. Third, all of these materials have excellent chemical durability. Besides, metal (Ag) is usually utilized for the solar reflector, and the dielectric is able to be utilized to adjust the visible transmittance and near-infrared reflectance by diminishing the surface plasma and lessening the metal layer's absorption. Both the material types and thickness variations enable the multilayer film to achieve the desired multispectral properties.

**2.3. Genetic Algorithm.** In Figure 2, the genetic algorithm is a biomimetic optimization approach that emulates the processes of selection, crossover, and mutation observed in biological genetics.<sup>48</sup> Commencing with a randomly generated initial population, the GA iteratively refines individuals, adapting them to the environment by employing genetic operators. Over the processes of optimization, this iterative process leads the population to evolve, ultimately converging toward an optimal solution within the specified parameter range.<sup>49,50</sup> To ensure a balance between diversity and inheritance, crossover rates and mutation rates were determined to be 0.7 and 0.0024, respectively. In this algorithm, every structure is treated as a unique design within a population of TNRs, undergoing sequential steps (namely, crossover, mutation, reselection, and refinement) to adjust the material types and thickness of each layer.

As shown in step (1) in Figure 2, a multilayer transparent NIR reflector is explored for color preservation using the mixed-integer GA to optimize the number of layers, material type, and layer thickness simultaneously. To guarantee that the GA

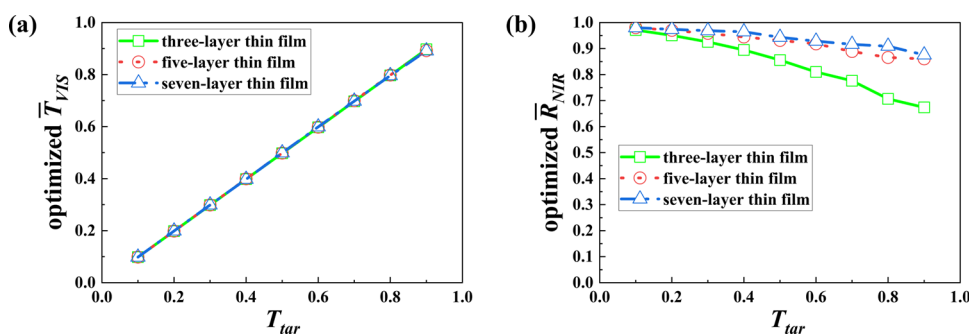


**Figure 3.** (a) Relationship between  $T_{tar}$  and optimized  $\bar{T}_{VIS}$  of 3, 5, and 7-layer multilayer film. (b) Relationship between  $T_{tar}$  and optimized  $\bar{R}_{NIR}$  of 3, 5, and 7-layer multilayer film.

achieves the optimal situation, we encode the candidate materials of each layer as  $m_i$ . The material of each layer was determined throughout the GA optimization process. Alongside the candidate material  $m_i$ , the thickness  $d_i$  is the other key parameter affecting the optical properties of the multilayer thin-film structure. In terms of optimizing efficiency and practical fabrication, the maximum number of layers in multilayers is set to 3, 5, and 7. If the intermediate TNR design contains two or more consecutive layers of the same material, then these identical layers actually represent a single layer. The range of each layer's thickness varies from 0 to 0.2  $\mu\text{m}$ . We began by producing 500 random TNR structures to form our original population. Besides, the process of optimization is terminated after reaching 1000 generations. The number of layers, material type, and layer thickness in the TNR are simultaneously optimized using the GA. The merit function (MF) is designed, as shown in eq 1. By minimizing the MF, the GA could optimize the TNR structure to achieve a flat visible transmittance and high average NIR reflectance.

$$MF = a \times \max(\text{RMSE}_{tar}, \text{RMSE}(T_{tar})) - b \times \bar{R}_{NIR} \quad (1)$$

$$\text{RMSE}_{tar} = c \times T_{tar} \quad (2)$$

$$\text{RMSE}(T_{tar}) = \frac{\sqrt{\sum_{j=1}^n (T_{VIS}(j) - T_{tar})^2}}{n} \quad (3)$$

$\text{RMSE}_{tar}$  is the target root mean squared error.  $\text{RMSE}(T_{tar})$  is the root mean squared error between visible transmittance ( $T_{VIS}$ ) and target transmittance ( $T_{tar}$ ).  $T_{tar}$  is the target transmittance, which ranges from 10 to 90% with an interval of 10%.  $\bar{R}_{NIR}$  is the average NIR reflectance from 0.78 to 2.5  $\mu\text{m}$ . The weights  $a$ ,  $b$ , and  $c$  have values of 100, 1, and 0.05% respectively.  $\bar{T}_{VIS}$  and  $\bar{R}_{NIR}$  are calculated by the TMM, which can be seen in Supporting Information SI3. The MF continuously decreases with the iterative evolution process of the population. In eq 1,  $\max(\text{RMSE}_{tar}, \text{RMSE}(T_{tar}))$  represents taking the maximum value between  $\text{RMSE}_{tar}$  and  $\text{RMSE}(T_{tar})$ . When  $\text{RMSE}(T_{tar})$  decrease to the  $\text{RMSE}_{tar}$ , the GA will no longer optimize  $\max(\text{RMSE}_{tar}, \text{RMSE}(T_{tar}))$  to minimize the value but instead optimize  $\bar{R}_{NIR}$  to make it as high as possible, ultimately achieving the minimum value of the MF.

After around 1000 generations, we succeed in keeping  $\text{RMSE}(T_{tar})$  to be  $\text{RMSE}_{tar}$  (for example,  $\text{RMSE}(10\%) = c \times T_{tar} = 0.05\% \times 10\% = 5 \times 10^{-5}$ , the more detailed information can be seen in Supporting Information SI4), which maintains the transmittance curve to be flat for color-preserving. The TNR structure consists of multilayer films, with the maximum number of layers set as 3, 5, and 7. For the maximum number of layers in

the multilayer set to 3, 5 and 7, the material type and layer thickness are optimized simultaneously, and the optimization process finally converged to  $\text{Al}_2\text{O}_3/\text{Ag}/\text{Al}_2\text{O}_3$ ,  $\text{Al}_2\text{O}_3/\text{Ag}/\text{Al}_2\text{O}_3/\text{Ag}/\text{Al}_2\text{O}_3$ , and  $\text{Al}_2\text{O}_3/\text{Ag}/\text{Al}_2\text{O}_3/\text{Ag}/\text{Al}_2\text{O}_3/\text{Ag}/\text{Al}_2\text{O}_3$ , which we called the dielectric-metal (DM) multilayer film or TNR. The details of the TNR are elaborated in Results and Discussion 3.1.

After realizing wavelength selectivity using the GA, the TNR structures have flat transmittance for color-preserving and high NIR reflectance for stopping the incident NIR solar radiation. Nevertheless, the optimized TNR has very low emittance, which is nearly close to zero. Moreover, incident visible sunlight carrying solar radiation makes our multilayer structure inevitably heat up, which hinders the cooling effect. Thus, a thermal emitter consisting of a 100- $\mu\text{m}$ -thick PDMS is positioned above the TNR, aiming to enhance the emission within the atmospheric window for radiative cooling. After combining the TNR and the PDMS, a CPRCW has emerged (Figure 1d). The refractive index of PDMS can be seen in Supporting Information SI2. However, the proposed radiative cooling window shows oscillation properties in the solar spectrum.<sup>33,35</sup> These oscillation properties do not exist in the solar spectrum of the individual TNR. They are caused by the interference effect between the TNR and PDMS. Thereby, the color of the transmitted light may not be preserved as a result of the oscillations, which means that the transmittance curve in the visible band is not flat.

As shown in step(2) in Figure 2, to reduce the impact of oscillation on color-preserving and enhance the emission within the atmospheric window, we repeatedly make use of the genetic algorithm to optimize the spectral properties of the CPRCW. In eq 1, we set the parameter  $c$  to 0.5% and  $T_{tar}$  to 10 and 90%. Because there are spectral oscillations in the proposed radiative cooling window, we cannot achieve a variance as small as that of a TNR structure. In other words, the transmittance curve of the color-preserving radiative cooling window cannot be as flat as that of the TNR. So, we are setting parameter  $c$  to 0.5% here, instead of the previous 0.05%. Parameters  $a$  and  $b$  remain unchanged, just like before. Utilizing the GA again, we accomplish the optimization, and the proposed CPRCW has been achieved. In other words, we succeed in keeping  $\text{RMSE}(T_{tar})$  to be  $\text{RMSE}_{tar}$ . Thus, the  $\bar{T}_{VIS}$  can reach  $T_{tar}$  with a very small variance, which is able to make the visible transmittance curve flat for color-preserving. Besides, when  $\bar{T}_{VIS}$  reaches 10 and 90%, the corresponding average NIR reflectance ( $\bar{R}_{NIR}$ ) is 91 and 86%, respectively. The details of the CPRCW are elaborated in Results and Discussion 3.2.



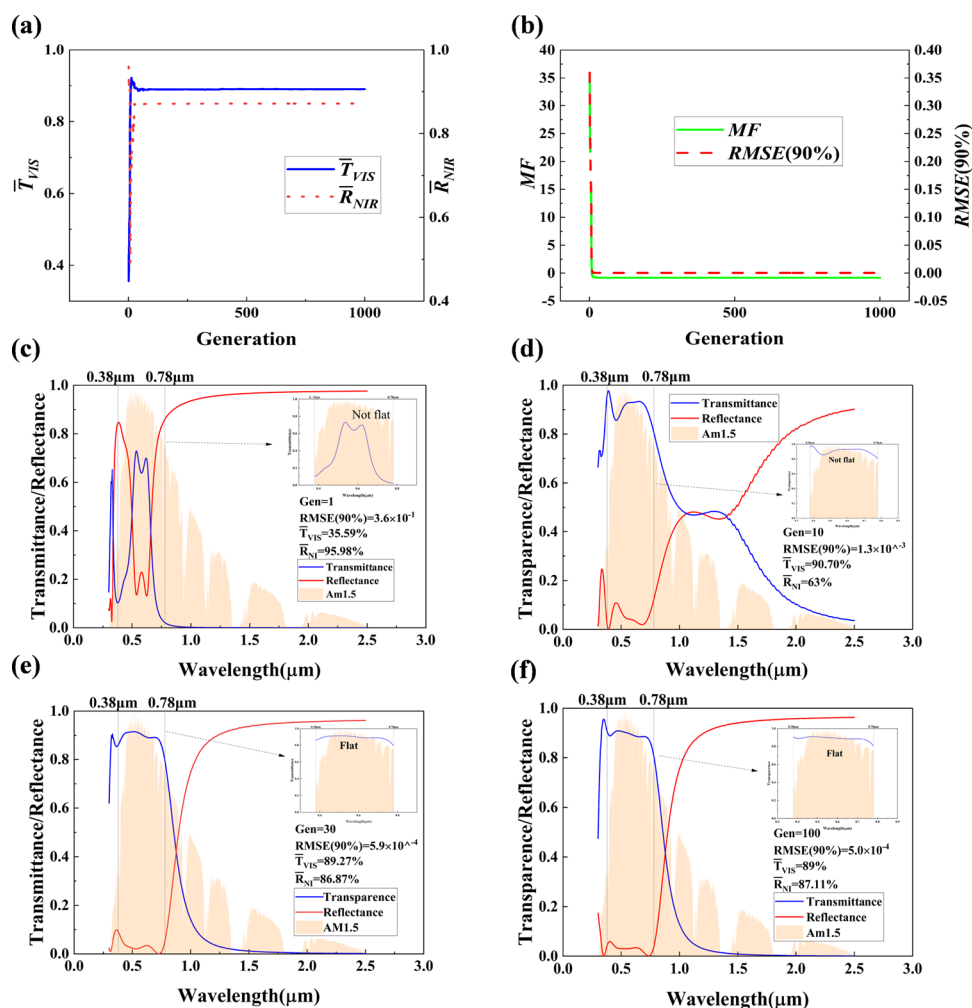


**Figure 4.** (a)  $\bar{T}_{VIS}$  and  $\bar{R}_{NIR}$  of TNR9 in each generation. (b) MF and RMSE(90%) of TNR9 in each generation. (c–f) Spectra of solar transmissivity and reflectance of the best TNR structures in the first, 10th, 30th, and 100th generations.

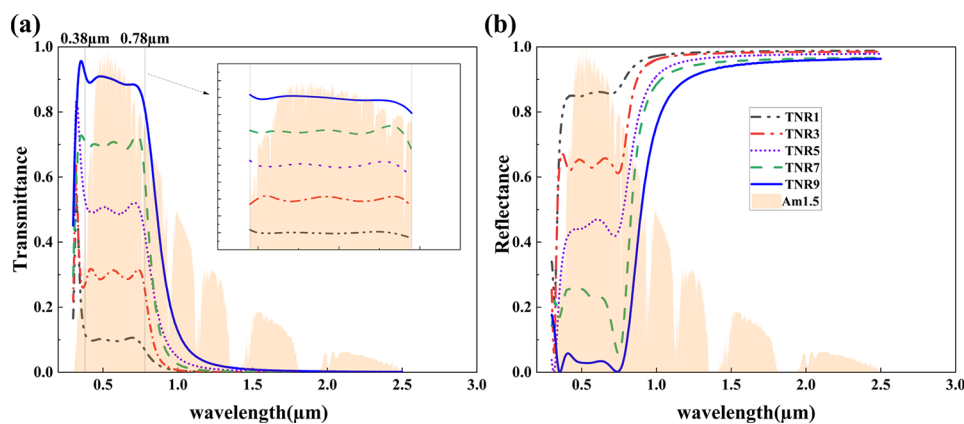


**Figure 5.** (a) Spectrum of transmittance of different TNRs whose  $\bar{T}_{VIS}$  reaches different  $T_{tar}$ . (b) Spectrum of reflectance of different TNRs whose  $\bar{T}_{VIS}$  reaches different  $T_{tar}$ .

### 3. RESULTS AND DISCUSSION

**3.1. Optimization of the Transparent Near-Infrared Reflector.** The TNR structure, wherein the maximum number of layers is 3, 5, and 7, is analyzed and compared in Figure 3a,b. In Figure 4a, we utilize the GA to keep the RMSE( $T_{tar}$ ) to be RMSE( $T_{tar}$ ), where  $T_{tar}$  ranges from 10 to 90% with a step-size of 10%. With a very small variance, we can make  $\bar{T}_{VIS}$  nearly reach

the target average transmittance ( $T_{tar}$ ) for 3, 5, and 7-layer DM multilayers. Subsequently, for an in-depth assessment of the optimal TNR, we utilize the GA to increase  $\bar{R}_{NIR}$  as high as possible, when we keep the  $\bar{T}_{VIS}$  nearly to  $T_{tar}$ . In Figure 4b, when we fix  $\bar{T}_{VIS}$  to the same  $T_{tar}$ ,  $\bar{R}_{NIR}$  increases as the film layer number increases from 3 to 7. This is because the more layers of film, the higher the reflectance.<sup>46,47</sup> In a word, the 7-layer DM

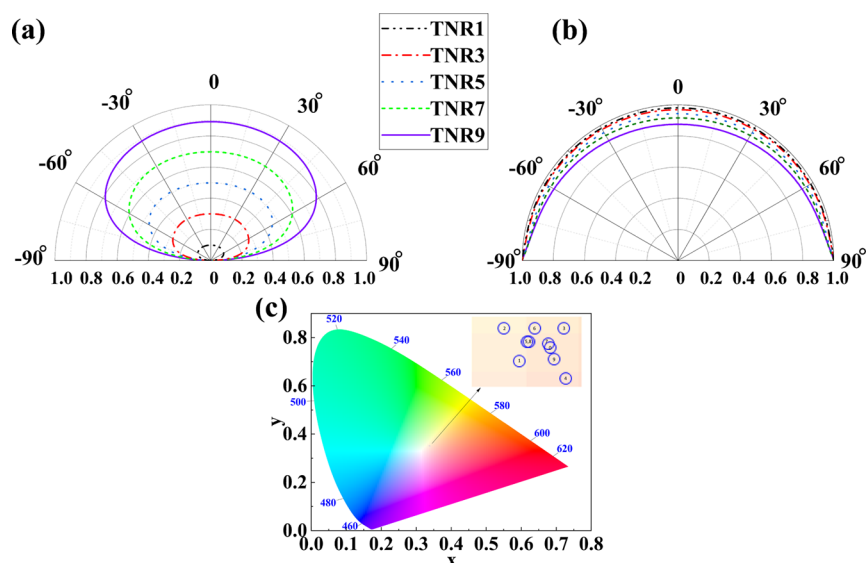


**Figure 6.** Spectrum of (a)  $\bar{T}_{\text{VIS}}$  and (b)  $\bar{R}_{\text{NIR}}$  of TNR with different  $T_{\text{tar}}$  as a function of incident angle. (c) Chromaticity diagrams of transmissive color of TNRs with different  $T_{\text{tar}}$ .

multilayer has the highest  $\bar{R}_{\text{NIR}}$  compared to the 3-layer and 5-layer DM multilayers when we keep the  $\bar{T}_{\text{VIS}}$  nearly to  $T_{\text{tar}}$  with a small variance. Thus, we choose the 7-layer  $\text{Al}_2\text{O}_3/\text{Ag}/\text{Al}_2\text{O}_3/\text{Ag}/\text{Al}_2\text{O}_3/\text{Ag}/\text{Al}_2\text{O}_3$  multilayer film structure as the transparent NIR reflector.

Now, we present the process of the optimization about the 7-layer TNR structure with  $\text{RMSE}(90\%) = 4.5 \times 10^{-4}$ . The details about other structures can be seen in [Supporting Information SI4](#). [Figure 4a,b](#) plots  $\bar{T}_{\text{VIS}}$ ,  $\bar{R}_{\text{NIR}}$ , MF, and  $\text{RMSE}(90\%)$  with the change of the generations. The decreases of both scores of MF and  $\text{RMSE}(90\%)$  demonstrate the effectiveness of the algorithm. The progress in solar transmissivity and infrared reflectance of the TNR structure across selected generations is portrayed in [Figure 4c–f](#), which shows the spectra of solar transmissivity and reflectance of the best TNR structures in the first, 10th, 30th, and 100th generations. Over the optimization period, we observe the  $\text{RMSE}(90\%)$  gradually decreases from  $3.6 \times 10^{-1}$  to  $4.5 \times 10^{-4}$ , which means that the transmittance curve in the visible band tends to be flat for preserving the color of the transmitted light. Therefore, the feasibility of genetic algorithms has been confirmed.

[Figure 5](#) shows the spectra of transmittance and reflectance of the TNRs. In [Figure 5a,b](#), we show the spectra of transmittance and relevant reflectance of TNR in a full wavelength range from 0.3 to  $2.5 \mu\text{m}$  when the  $\bar{T}_{\text{VIS}}$  is fixed to  $T_{\text{tar}}$ . For example, TNR1 means the TNR whose  $\text{RMSE}(10\%) = c \times T_{\text{tar}} = 0.05\% \times 10\% = 5 \times 10^{-5}$ . The more detailed information can be seen in [Supporting Information SI4](#). In [Figure 5a](#), we can see that the transmittance curve in the visible band is nearly flat, which helps preserve the composition of the transmitted light. [Figure 5b](#) shows the reflectance of the 7-layer TNR. When the  $\bar{T}_{\text{VIS}}$  is fixed from 10 to 90% with a step-size of 20%,  $\bar{R}_{\text{NIR}}$  is 98, 97, 94, 92, and 87%. It is obvious that average NIR reflectance increases as average visible transmittance decreases, which is in accordance with the facts. The 7-layer TNR structure ( $\text{Al}_2\text{O}_3/\text{Ag}/\text{Al}_2\text{O}_3/\text{Ag}/\text{Al}_2\text{O}_3/\text{Ag}/\text{Al}_2\text{O}_3$ ) can be seen as composed of three DMD structures with different reflection and transmission bands. The selective broadband reflection and transmission achieved by the 7-layer TNR structure attributes to the superposition of these reflection and transmission bands of the DMD structures.

To study the optimized transparent NIR reflector's consistency across varying incident angles, we plot the  $\bar{T}_{\text{VIS}}$  and  $\bar{R}_{\text{NIR}}$  when  $\bar{T}_{\text{VIS}}$  at normal incidence is nearly fixed between 10 and 90% with a step-size of 20%, against the oblique incident angle ( $\theta$ ). In [Figure 6a,b](#), we have presented the spectrally  $\bar{T}_{\text{VIS}}$  and  $\bar{R}_{\text{NIR}}$  of TNR structures. The transmittance and reflectance shown here are the average for both polarizations at normal incidence. As depicted in [Figure 6a](#), the average visible transmissivity over both polarizations remains consistent for  $\theta$  less than around  $60^\circ$ . When the incident angle exceeds  $60^\circ$ , the average visible transmittances have evident drops. Furthermore, as shown in [Figure 6b](#), the average NIR reflectance has no obvious changes with the various angles. When the average visible transmittance is nearly fixed from 10 to 90% with a step-size of 20% at normal incidence, the average NIR reflectance is 98, 97, 94, 91, and 87%. The detailed information can be seen in [Supporting Information SI4](#). Furthermore, as  $\theta$  increases from 0 to  $90^\circ$ , the average NIR reflectance reaches nearly 100%. Therefore, under the condition of oblique incidence, the 7-layer TNR structure ( $\text{Al}_2\text{O}_3/\text{Ag}/\text{Al}_2\text{O}_3/\text{Ag}/\text{Al}_2\text{O}_3/\text{Ag}/\text{Al}_2\text{O}_3$ ) can still maintain stable visible light transmittance and near-infrared reflectance and has minimal dependence on the incident angle.

In the field of transparent NIR reflectors, we first keep the root-mean-square of average visible transmittance at  $0.05\% \times T_{\text{tar}}$ , which aims to maintain the visible transmittance curve to be flat for color-preserving. Subsequently, we take advantages of the genetic algorithm to increase the average NIR reflectance as far as possible, when average visible transmittance is fixed from 10 to 90% with a step-size of 20%. In a nutshell, we utilize the genetic algorithm to design the TNR which has flat visible transmittance and high NIR reflectance as much as possible.

After the TNR achieved by genetic algorithm optimization results in a notable flat transmission within the visible solar spectrum, we studied how the optimized TNR affects the creation of transmissive color at normal incidence. The chromaticity diagrams of transmissive color about transparent NIR reflector structures with different average visible transmittances are shown in [Figure 6c](#). The relevant RGB and colors of each visible transmitted light are also listed in [Table 1](#). The calculation method of RGB is indicated in [Supporting](#)

**Table 1. Corresponding Transmissive Colors and the Value of RGB for Different TNRs**

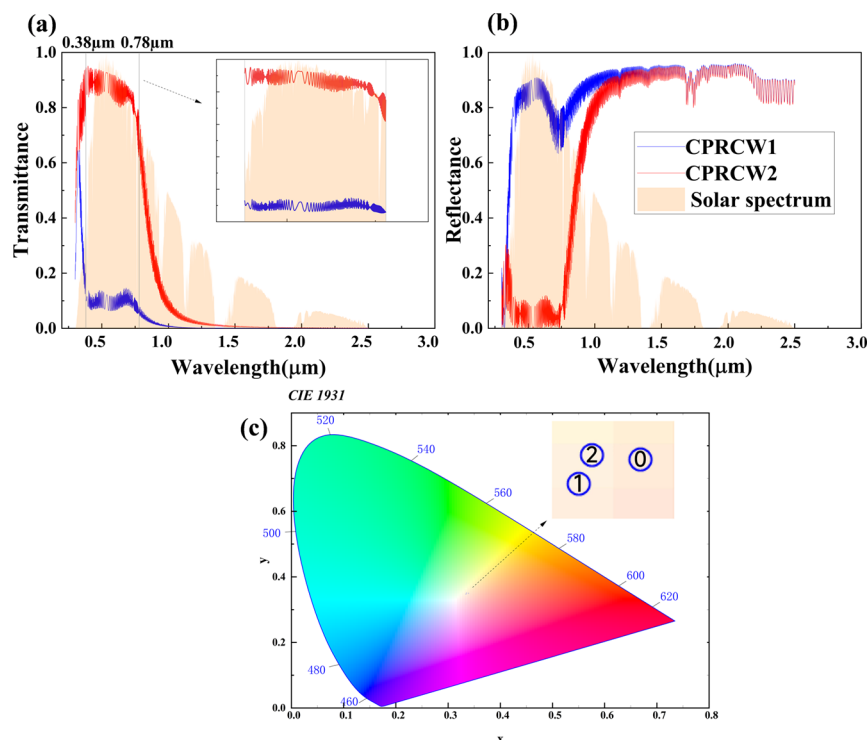
Number		RGB(x,y,Y)	Color	RGB(X,Y,Z)	Color
0	sunlight	(0.3391,0.3501,100)		(96.3228, 99.4463, 88.3114)	
1	TNR1	(0.3363,0.3485,100)		(9.398, 9.739, 8.8044)	
2	TNR2	(0.3348,0.3527,100)		(19.1784, 20.1657, 17.5154)	
3	TNR3	(0.3403,0.3527,100)		(29.1864, 30.2454, 26.3251)	
4	TNR4	(0.3405,0.3463,100)		(39.0410, 39.7102, 35.9127)	
5	TNR5	(0.3369,0.351,100)		(47.4038, 49.3860, 43.9052)	
6	TNR6	(0.3377,0.3527,100)		(58.1289, 59.8336, 53.3592)	
7	TNR7	(0.339,0.3506,100)		(29.1864, 30.2454, 26.3251)	
8	TNR8	(0.3372,0.351,100)		(76.1695, 79.2824, 70.4207)	
9	TNR9	(0.3395,0.348,100)		(86.2159, 89.4861, 79.7964)	

**Information S15.** “0” refers to the solar spectrum. The numbers from ‘1’ to ‘9’ correspond to TNR1 through TNR9. When the number ranges from 1 to 9, the color of sunlight passing through TNR is shown in Table 1. In the last column of Table 1, the color of sunlight passing through the transparent near-infrared reflector is unusual because the brightness  $Y$  is not equal to 100. The  $Y$  value represents the luminance of the light (or the measure of its brightness), and not all light sources or light passing through filters will have a maximum luminance value of 100. A  $Y$  value not equal to 100 simply means that the brightness of that light source is not the maximum luminance that the color space can describe. In order to provide a unified standard for the color space, allowing for comparison and conversion of different colors on the same scale, we normalize the  $Y$  value to 100. Additionally, we calculate the corresponding  $x$  and  $y$  values, as shown in the fourth column of Table 1.  $x$  and  $y$  are chromaticity coordinates derived from the  $X$ ,  $Y$ , and  $Z$  coordinates. They are used to describe the hue and saturation of the colors.

The CIE-1931 chromaticity, as seen in Figure 6c, displays the comparison of the sunlight colors to the transmissive colors. As the RMSE between  $T_{\text{VIS}}$  and  $T_{\text{tar}}$  is fixed to be a small value, there’s a slight variance observed between the transmissive colors and sunlight colors, attributed to the flat transmittance curve of the TNR in the visible band. This is consistent with Figure 5a whose visible transmittance curve is flat for color-preserving.

### 3.2. Color-Preserving Radiative Cooling Window.







Utilizing TMM, we perform a calculation of the transmittance and reflectance over an ultrabroadband wavelength range from 0.3 to 2.5  $\mu\text{m}$  with a wavelength step-size of 1 nm, as shown in Figure 7a,b. As Figure 7a reveals, although certain discernible oscillations arise due to the interference of the thin film, we have utilized the GA to make the visible transmittance as flat as



**Figure 7.** Spectrum of transmittance (a) and reflectance (b) of CPRCW1 and CPRCW2. (c) Chromaticity diagrams of the transmissive color of CPRCW1 and CPRCW2.

possible for color-preserving where the CPRCW has been achieved. In Figure 7, CPRCW1 and CPRCW2 represent the radiative cooling window whose  $\bar{T}_{\text{VIS}}$  reaches 10 and 90%, respectively, with a small variance. We now analyze the color of transmissive sunlight which passes through the CPRCW. The CIE-1931 chromaticity coordinates of the color of transmissive light and sunlight for normal incidence are calculated, as shown in Figure 7c. The calculation method of RGB is indicated by Supporting Information S15. As seen in Table 2, number 0

**Table 2. Corresponding Transmissive Colors and the Value of RGB for CPRCW1 and CPRCW2**

Number		RGB(x,y,Y)	Color	RGB(X,Y,Z)	Color
0	sunlight	(0.3391, 0.3501,100)		(96.3228, 99.4463, 88.3114)	
1	CPRC W1	(0.3341, 0.3474,100)		(8.8293, 9.1789, 8.4171)	
2	CPRC W2	(0.3353, 0.3506,100)		(84.0250, 87.8783, 78.7191)	

represents the color of sunlight, and numbers 1 and 2 mean CPRCW1 and CPRCW2, whose  $\bar{T}_{\text{VIS}}$  reach 10 and 90%, respectively, with a very small variance. When the number ranges from 1 to 2, the color of sunlight passing through the CPRCW is shown in Table 2. Although the  $T_{\text{tar}}$  of CPRCW1 and CPRCW2 are 10 and 90%, respectively, due to variance, their actual  $\bar{T}_{\text{VIS}}$  are 9.5 and 86% in accordance. In Figure 7c, the flat visible transmittance curve of the color-preserving radiative cooling window preserves the original color of the transmissive sunlight, which means that no obvious color distortion can be observed.

After reducing the impact of oscillation on color-preserving, we now present and analyze the effect of radiative cooling. As shown in Figure 8, the emissions of CPRCW1 and CPRCW2 in the atmospheric window are almost the same because they both have the PDMS of the same thickness, which plays a very key role in MIR emission. Furthermore, the designed CPRCW1 and CPRCW2 display a broadband and high average mid-infrared emittance of 95% at the atmospheric transparent window, while TNR1 and TNR9 whose  $\bar{T}_{\text{VIS}}$  reach 10 and 90% with a very small

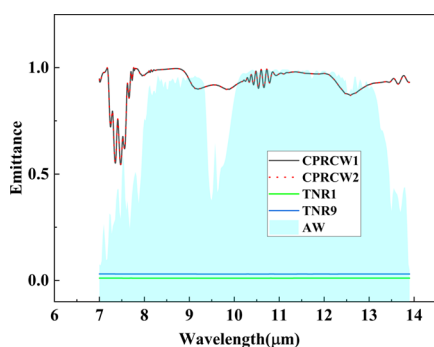


**Figure 8.** Spectrum of emittance of CPRCW1, CPRCW2, TNR1, and TNR9.

variance have a very low MIR emittance (nearly to zero). The broadband and high emittance (Figure 8) of the designed CPRCW1 and CPRCW2 align well with the ideal  $E$  values, as shown in Figure 1b. Therefore, the transparent NIR reflector is inevitable to heat up because of the low MIR emittance in theory. This strong MIR emission of the proposed CPRCW is mainly attributed to the 100- $\mu\text{m}$ -thick PDMS, which serves as an MIR thermal emitter.<sup>24</sup> To study the consistency of the CPRCW and TNR across varying incident angles, we plot the  $\bar{E}_{\text{AW}}$  against the oblique incident angle ( $\theta$ ) in Figure 9. The emittance shown

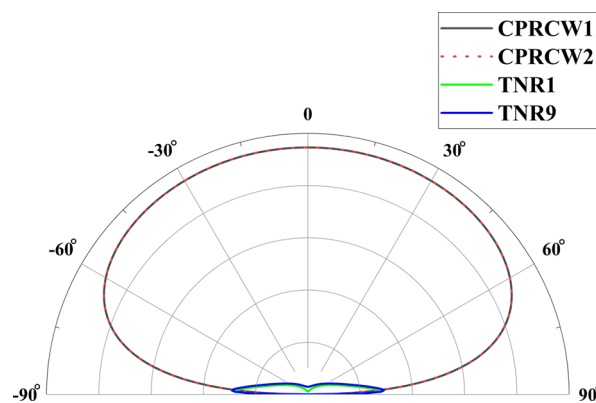


**Figure 9.** Spectrum of  $\bar{E}_{\text{AW}}$  of CPRCW and TNR with different  $T_{\text{tar}}$  values as a function of incident angle.

here is the average for both polarizations at normal incidence. As depicted in Figure 9,  $\bar{E}_{\text{AW}}$  of CPRCW1 and CPRCW2 over both polarizations remains consistent for  $\theta$  less than around 60°. When the incident angle exceeds 60°, the  $\bar{E}_{\text{AW}}$  of CPRCW1 and CPRCW2 has evident drops. As same as Figure 8, the  $\bar{E}_{\text{AW}}$  of CPRCW1 and CPRCW2 in Figure 9 are almost the same because they both have the PDMS of the same thickness. In Figure 9,  $\bar{E}_{\text{AW}}$  of TNR1 and TNR9 remain low across varying incident angles, which means poor performance of radiative cooling. Accordingly, the proposed CPRCW demonstrates a robust and elevated emissivity within the atmospheric window across a variety of angles, rendering it exceptionally conducive to applications in radiative cooling windows. This attribute enhances its utility in maintaining thermal efficiency and environmental adaptability in sustainable building designs.

To further illustrate the importance of emissivity on the cooling performance, in Figure 10, based on eq 1 in Supporting Information S11, we plot the cooling power  $P_{\text{cool}}$  as a function of the temperature  $\Delta T_{\text{eq}}$  ( $\Delta T_{\text{eq}} = T_{\text{eq}} - T_{\text{amb}}$ ). The equilibrium temperature  $T_{\text{eq}}$ , where  $P_{\text{cool}}(T_{\text{eq}}) = 0$ , defines the lowest temperature that CPRCW can reach. Here, we assume that  $T_{\text{amb}} = 300$  K. The lower the value of  $\Delta T_{\text{eq}}$ , the better the cooling effect of the structure. As shown in Figure 7a,b, CPRCW1 and CPRCW2 exhibit a flat visible transmissivity and an ultrahigh NIR reflectance. Meanwhile, they achieve a highly selective thermal emissivity, which is closely matched with the transparent atmospheric window, as shown in Figure 8. The influence of transmissivity on cooling power and equilibrium temperature is also analyzed theoretically. In Figure 10, we show the cooling power as a function of  $\Delta T_{\text{eq}}$  for different  $h_c$  values ( $h_c = 0$  W/m<sup>2</sup>/K,  $h_c = 6$  W/m<sup>2</sup>/K, and  $h_c = 12$  W/m<sup>2</sup>/K).<sup>51</sup>  $h_c$  is a nonradiative heat coefficient,<sup>9</sup> which has been described in Supporting Information S11. In addition, as can be seen from Figure 10, the optimized CPRCW structure in this paper has higher cooling power than the glass window with equal thickness. For a



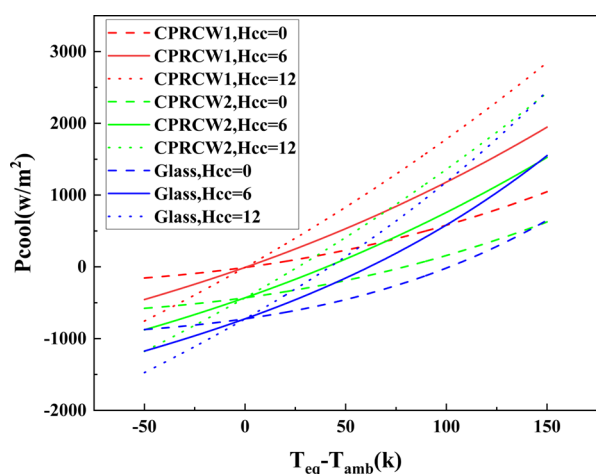


**Figure 10.** Cooling power as a function of the temperature difference at different  $h_c$  values.  $T_{\text{amb}} = 300$  K is used for all of the plots.

different  $h_c$ , the proposed CPRCW always exhibits much lower  $\Delta T_{\text{eq}}$  than the equal-thickness glass window (as listed in Table 3). When the  $\bar{T}_{\text{VIS}}$  is fixed to 10% (CPRCW1), the drop of

**Table 3.** Value of  $\Delta T_{\text{eq}}$  ( $T_{\text{eq}} - T_{\text{amb}}$ ) with Different Structures for  $P_{\text{cool}} = 0$  W/m<sup>2</sup>

	$h_c = 0$ W/m <sup>2</sup> /K	$h_c = 6$ W/m <sup>2</sup> /K	$h_c = 12$ W/m <sup>2</sup> /K
CPRCW1 (K)	2	0.8	0.5
CPRCW2 (K)	79.2	40.5	26.4
glass (K)	101.5	61.7	42.2

temperature is 99.5, 60.9, and 41.7 K compared with the equal-thickness glass for  $h_c = 0, 6,$  and  $12$  W/m<sup>2</sup>/K. When the  $\bar{T}_{\text{VIS}}$  is fixed to 90% (CPRCW2), the drop of temperature is 22.3, 21.2, and 15.8 K compared with the equal-thickness glass window for  $h_c = 0, 6,$  and  $12$  W/m<sup>2</sup>/K.

#### 4. CONCLUSIONS

In conclusion, we designed a color-preserving radiative cooling window that can preserve color and lower the temperature. Through our systematic design approaches, based on the genetic algorithm and transfer matrix method, we combine solar energy management (wavelength-dependent transmission/reflection) and radiative cooling in a planar multilayer stack of dielectric and metal layers. Unlike most previous designs, our designed transparent cooling window has broadband and flat transmittance for color-preserving in the visible band and high NIR reflectance to block much of the NIR light components. This is achieved by utilizing the GA to optimize the CPRCW to fix average visible transmittance to 10 and 90% with minimal variance, and the relative average NIR reflectances are 91 and 86%. Although the  $T_{\text{tar}}$  of CPRCW1 and CPRCW2 is 10 and 90% respectively, due to variance, their actual  $\bar{T}_{\text{VIS}}$  are 9.5 and 86% in accordance. Moreover, the broadband thermal emission was demonstrated using a uniform 100- $\mu\text{m}$ -thick PDMS layer placed on the TNR, which shows high thermal emissivity (95%) across the broad mid-IR range. By combining the TNR with a 100- $\mu\text{m}$ -thick PDMS, a color-preserving radiative cooling window has been achieved by the GA. Compared with a glass window with equal thickness, the drop of temperature caused by CPRCW1 is 99.5, 60.9, and 41.7 K for  $h_c = 0$  W/m<sup>2</sup>/K,  $h_c = 6$  W/m<sup>2</sup>/K, and  $h_c = 12$  W/m<sup>2</sup>/K, and the drop of temperature caused

by CPRCW2 is 22.3, 21.2, and 15.8 K for  $h_c = 0$  W/m<sup>2</sup>/K,  $h_c = 6$  W/m<sup>2</sup>/K, and  $h_c = 12$  W/m<sup>2</sup>/K, respectively. The structure proposed in this work achieves different transmittances ranging from 10 to 90% and could be used in low-visibility (such as helmets, shading visors, or goggles) and high-visibility (such as windows of buildings and cars) radiative cooling.

#### ■ ASSOCIATED CONTENT

##### Supporting Information

The Supporting Information is available free of charge at <https://pubs.acs.org/doi/10.1021/acsomega.4c01792>.

Radiative cooling formula, refractive index of materials, transfer matrix method, thickness of designed CPRCW and TNR, and color calculation and conversion (PDF)

#### ■ AUTHOR INFORMATION

##### Corresponding Authors

**Shujing Chen** – School of Materials Science and Technology, China University of Geosciences, Beijing 100083, China; Email: [chenshujing@cugb.edu.cn](mailto:chenshujing@cugb.edu.cn)

**Chengyou Lin** – College of Mathematics and Physics, Beijing University of Chemical Technology, Beijing 100029, China; [orcid.org/0000-0003-2257-4147](https://orcid.org/0000-0003-2257-4147); Email: [cylin@buct.edu.cn](mailto:cylin@buct.edu.cn)

##### Author

**Guowei Liu** – College of Mathematics and Physics, Beijing University of Chemical Technology, Beijing 100029, China

Complete contact information is available at:

<https://pubs.acs.org/10.1021/acsomega.4c01792>

##### Notes

The authors declare no competing financial interest.

#### ■ ACKNOWLEDGMENTS

This work was supported by the National Natural Science Foundation of China (61805007).

#### ■ REFERENCES

- (1) Lelieveld, J.; Klingmüller, K.; Pozzer, A.; Burnett, R. T.; Haines, A.; Ramanathan, V. Proceedings of the National Academy of Sciences of the United States of America. *Proc. Natl. Acad. Sci. U.S.A.* **2019**, *116* (15), 7192–7197.
- (2) Ghosh, A.; Norton, B. Advances in Switchable and Highly Insulating Autonomous (Self-Powered) Glazing Systems for Adaptive Low Energy Buildings. *Renew. Energy* **2018**, *126*, 1003–1031.
- (3) Kim, J.; Baek, S.; Park, J. Y.; Kim, K. H.; Lee, J. L. Photonic Multilayer Structure Induced High near-Infrared (Nir) Blockage as Energy-Saving Window. *Small* **2021**, *17* (29), No. 2100654.
- (4) Zhang, K.; Zhao, D. L.; Yin, X. B.; Yang, R. G.; Tan, G. Energy Saving and Economic Analysis of a New Hybrid Radiative Cooling System for Single-Family Houses in the USA. *Appl. Energy* **2018**, *224*, 371–381.
- (5) Dalapati, G. K.; Masudy-Panah, S.; Chua, S. T.; Sharma, M.; Wong, T. I.; Tan, H. R.; Chi, D. Z. Color Tunable Low Cost Transparent Heat Reflector Using Copper and Titanium Oxide for Energy Saving Application. *Sci. Rep.* **2016**, *6*, 20182.
- (6) Piccolo, A.; Marino, C.; Nucara, A.; Pietrafesa, M. Energy Performance of an Electrochromic Switchable Glazing: Experimental and Computational Assessments. *Energy Build.* **2018**, *165*, 390–398.
- (7) Salamati, M.; Kamyabjou, G.; Mohamadi, M.; Taghizade, K.; Kowsari, E. Preparation of Tio2@W-Vo2 Thermochromic Thin Film for the Application of Energy Efficient Smart Windows and Energy

Modeling Studies of the Produced Glass. *Constr. Build. Mater.* **2019**, *218*, 477–482.

(8) Ahn, B. L.; Kim, J. H.; Jang, C. Y.; Leigh, S. B.; Jeong, H. Window Retrofit Strategy for Energy Saving in Existing Residences with Different Thermal Characteristics and Window Sizes. *Build. Serv. Eng. Res. Technol.* **2016**, *37* (1), 18–32.

(9) Zhou, Z. G.; Wang, X.; Ma, Y. G.; Hu, B.; Zhou, J. Transparent Polymer Coatings for Energy-Efficient Daytime Window Cooling. *Cell Rep. Phys. Sci.* **2020**, *1* (11), No. 100231.

(10) Sun, C.; Xia, R. X.; Shi, H.; Yao, H. F.; Liu, X.; Hou, J. H.; Huang, F.; Yip, H. L.; Cao, Y. Heat-Insulating Multifunctional Semitransparent Polymer Solar Cells. *Joule* **2018**, *2* (9), 1816–1826.

(11) Huang, T. Z.; Chen, Q. X.; Huang, J. H.; Lu, Y. H.; Xu, H.; Zhao, M.; Xu, Y.; Song, W. J. Scalable Colored Subambient Radiative Coolers Based on a Polymer-Tamm Photonic Structure. *ACS Appl. Mater. Interfaces* **2023**, *15* (12), 16277–16287.

(12) Kou, Z.; Wang, J. H.; Tong, X. R.; Lei, P. Y.; Gao, Y.; Zhang, S. Y.; Cui, X. P.; Wu, S. X.; Cai, G. F. Multi-Functional Electrochromic Energy Storage Smart Window Powered by Cztss Solar Cell for Intelligent Managing Solar Radiation of Building. *Sol. Energy Mater. Sol. Cells* **2023**, *254*, No. 112273.

(13) Yin, H. Y.; Fan, C. Z. Ultra-Broadband Thermal Emitter for Daytime Radiative Cooling with Metal-Insulator-Metal Metamaterials. *Chin. Phys. Lett.* **2023**, *40* (7), No. 077801.

(14) Raman, A. P.; Abou Anoma, M.; Zhu, L. X.; Rephaeli, E.; Fan, S. H. Passive Radiative Cooling Below Ambient Air Temperature under Direct Sunlight. *Nature* **2014**, *515* (7528), 540–544.

(15) Guan, Q. S.; Raza, A.; Mao, S. S.; Vega, L. F.; Zhang, T. J. Machine Learning-Enabled Inverse Design of Radiative Cooling Film with on-Demand Transmissive Color. *ACS Photonics* **2023**, *10* (3), 715–726.

(16) Li, B.; Hu, J. Q.; Chen, C. H.; Hu, H. R.; Zhong, Y. T.; Song, R. C.; Cao, B. Y.; Peng, Y. Q.; Xia, X. S.; Chen, K.; et al. Theoretical Study of a Highly Fault-Tolerant and Scalable Adaptive Radiative Cooler. *Nanophotonics* **2024**, *13* (5), 725–736.

(17) Zhu, L.; Raman, A.; Wang, K. X.; Anoma, M. A.; Fan, S. Radiative Cooling of Solar Cells. *Optica* **2014**, *1* (1), 32–38.

(18) Raman, A. P.; Li, W.; Fan, S. Generating Light from Darkness. *Joule* **2019**, *3* (11), 2679–2686.

(19) Wang, S.; Wu, Y. J.; Pu, M. B.; Xu, M. F.; Zhang, R. Y.; Yu, T.; Li, X.; Ma, X. L.; Su, Y. J.; Tai, H. L.; et al. A Versatile Strategy for Concurrent Passive Daytime Radiative Cooling and Sustainable Energy Harvesting. *Small* **2024**, *20* (6), No. 2305706.

(20) Wu, Y. J.; Wang, S.; Zhang, R. Y.; Yu, T.; Xu, M. F.; Li, X.; Pu, M. B.; Ma, X. L.; Guo, Y. C.; Su, Y. J.; et al. A Novel Multifunctional Photonic Film for Colored Passive Daytime Radiative Cooling and Energy Harvesting. *Small* **2024**, No. 2308661.

(21) Fan, C. H.; Long, Z. W.; Zhang, Y. X.; Mensah, A.; He, H. F.; Wei, Q. F.; Lv, P. F. Robust Integration of Energy Harvesting with Daytime Radiative Cooling Enables Wearing Thermal Comfort Self-Powered Electronic Devices. *Nano Energy* **2023**, *116*, No. 108842.

(22) Park, C.; Lee, W.; Park, C.; Park, S.; Lee, J.; Kim, Y. S.; Yoo, Y. Efficient Thermal Management and All-Season Energy Harvesting Using Adaptive Radiative Cooling and a Thermoelectric Power Generator. *J. Energy Chem.* **2023**, *84*, 496–501.

(23) Xi, W.; Liu, Y. D.; Zhao, W. X.; Hu, R.; Luo, X. B. Colored Radiative Cooling: How to Balance Color Display and Radiative Cooling Performance. *Int. J. Therm. Sci.* **2021**, *170*, No. 107172.

(24) Jin, Y.; Jeong, Y.; Yu, K. Infrared-Reflective Transparent Hyperbolic Metamaterials for Use in Radiative Cooling Windows. *Adv. Funct. Mater.* **2022**, *33* (1), No. 2207940.

(25) Kim, M.; Lee, D.; Son, S.; Yang, Y.; Lee, H.; Rho, J. Visibly Transparent Radiative Cooler under Direct Sunlight. *Adv. Opt. Mater.* **2021**, *9* (13), No. 2002226.

(26) Zhang, X. P.; Li, X.; Wang, F. Q.; Yuan, W. Z.; Cheng, Z. M.; Liang, H. X.; Yan, Y. Y. Low-Cost and Large-Scale Producing Biomimetic Radiative Cooling Glass with Multiband Radiative Regulation Performance. *Adv. Opt. Mater.* **2022**, *10* (23), No. 2202031.

(27) Wang, S. C.; Dong, Y. T.; Li, Y. B.; Ryu, K.; Dong, Z. L.; Chen, J.; Dai, Z. D.; Ke, Y. J.; Yin, J.; Long, Y. A Solar/Radiative Cooling Dual-Regulation Smart Window Based on Shape-Morphing Kirigami Structures. *Mater. Horiz.* **2023**, *10* (10), 4243–4250.

(28) Pérez-Escudero, J. M.; Torres-García, A. E.; Lezaun, C.; Caggiano, A.; Peralta, I.; Dolado, J. S.; Beruete, M.; Liberal, I. Suppressed-Scattering Spectral Windows for Radiative Cooling Applications. *Opt. Express* **2023**, *31* (4), 6314–6326.

(29) Lee, K. W.; Lim, W.; Jeon, M. S.; Jang, H.; Hwang, J.; Lee, C. H.; Kim, D. R. Visibly Clear Radiative Cooling Metamaterials for Enhanced Thermal Management in Solar Cells and Windows. *Adv. Funct. Mater.* **2022**, *32* (1), No. 2105882.

(30) Tian, Y. P.; Liu, X. J.; Wang, Z. Q.; Li, J. S.; Mu, Y.; Zhou, S. Y.; Chen, F. Q.; Minus, M. L.; Xiao, G.; Zheng, Y. Subambient Daytime Cooling Enabled by Hierarchically Architected All-Inorganic Metapaper with Enhanced Thermal Dissipation. *Nano Energy* **2022**, *96*, No. 107085.

(31) Wang, J.; Sun, J. Y.; Guo, T. T.; Zhang, H.; Xie, M.; Yang, J. B.; Jiang, X. P.; Chu, Z. Y.; Liu, D. Q.; Bai, S. X. High-Strength Flexible Membrane with Rational Pore Architecture as a Selective Radiator for High-Efficiency Daytime Radiative Cooling. *Adv. Mater. Technol.* **2022**, *7* (1), No. 2100528.

(32) Yue, X. J.; Wu, H.; Zhang, T.; Yang, D. Y.; Qiu, F. X. Superhydrophobic Waste Paper-Based Aerogel as a Thermal Insulating Cooler for Building. *Energy* **2022**, *245*, No. 123287.

(33) Dang, S. C.; Wang, X. J.; Ye, H. An Ultrathin Transparent Radiative Cooling Photonic Structure with a High NIR Reflection. *Adv. Mater. Interfaces* **2022**, *9* (30), No. 2201050.

(34) Li, X. S.; Xu, H. L.; Yang, Y. C.; Li, F. X.; Ramakrishna, S.; Yu, J. Y.; Ji, D. X.; Qin, X. H. Selective Spectral Absorption of Nanofibers for Color-Preserving Daytime Radiative Cooling. *Mater. Horiz.* **2023**, *10* (7), 2487–2495.

(35) Zhu, L. X.; Raman, A.; Fan, S. H. Color-Preserving Daytime Radiative Cooling. *Appl. Phys. Lett.* **2013**, *103* (22), No. 223902.

(36) Lin, Z. N.; Chen, S. J.; Lin, C. Y. Sensitivity Improvement of a Surface Plasmon Resonance Sensor Based on Two-Dimensional Materials Hybrid Structure in Visible Region: A Theoretical Study. *Sensors* **2020**, *20* (9), 2445.

(37) Lin, C. Y.; Chen, S. J. Design of High-Performance Au-Ag-Dielectric-Graphene Based Surface Plasmon Resonance Biosensors Using Genetic Algorithm. *J. Appl. Phys.* **2019**, *125* (11), No. 113101.

(38) Yeh, P.; Hendry, M. Optical Waves in Layered Media. *Phys. Today* **1990**, *43* (1), 77–78.

(39) Yang, S.; Chen, S. J.; Lin, C. Y. Design of Reflective Phase Retarders in the Extreme Ultraviolet Based on Chirped Mo/Si Multilayer Mirrors. *J. Synchrotron Radiat.* **2021**, *28*, 1437–1443.

(40) Shi, Y.; Li, W.; Raman, A.; Fan, S. H. Optimization of Multilayer Optical Films with a Memetic Algorithm and Mixed Integer Programming. *ACS Photonics* **2018**, *5* (3), 684–691.

(41) Zaman, M. A. Photonic Radiative Cooler Optimization Using Taguchi's Method. *Int. J. Therm. Sci.* **2019**, *144*, 21–26.

(42) Yang, H. H. U.; D'Archangel, J.; Sundheimer, M. L.; Tucker, E.; Boreman, G. D.; Raschke, M. B. Optical Dielectric Function of Silver. *Phys. Rev. B* **2015**, *91* (23), No. 235137.

(43) DeVore, J. R. Refractive Indices of Rutile and Sphalerite. *J. Opt. Soc. Am.* **1951**, *41* (6), 416–419.

(44) Zhang, X. N.; Qiu, J.; Li, X. C.; Zhao, J. M.; Liu, L. H. Complex Refractive Indices Measurements of Polymers in Visible and near-Infrared Bands. *Appl. Opt.* **2020**, *59* (8), 2337–2344.

(45) Zhang, X. N.; Qiu, J.; Zhao, J. M.; Li, X. C.; Liu, L. H. Complex Refractive Indices Measurements of Polymers in Infrared Bands. *J. Quant. Spectrosc. Radiat. Transfer* **2020**, *252*, No. 107063.

(46) Kecebas, M. A.; Menguc, M. P.; Kosar, A.; Sendur, K. Passive Radiative Cooling Design with Broadband Optical Thin-Film Filters. *J. Quant. Spectrosc. Radiat. Transfer* **2017**, *198*, 179–186.

(47) Mabchour, G.; Benlattar, M.; Saadouni, K.; Mazroui, M. Daytime Radiative Cooling Purposes with Selective Multilayer Design Based on Ta<sub>2</sub>O<sub>5</sub>. *Optik* **2020**, *214*, No. 164811.

(48) Zhang, L. Y.; Zhang, W. J.; Liu, Y. B.; Liu, L. H. Three-Layered Thin Films for Simultaneous Infrared Camouflage and Radiative Cooling. *Materials* **2023**, *16* (11), 4188.

(49) Peng, L.; Liu, D.; Cheng, H.; Zhou, S.; Zu, M. A Multilayer Film Based Selective Thermal Emitter for Infrared Stealth Technology. *Adv. Opt. Mater.* **2018**, *6* (23), No. 1801006.

(50) Yang, M. Y.; Zhou, M.; Yu, J. W.; Zhang, Y. B.; Xu, B. Y.; Cheng, W. J.; Li, X. Y. Infrared and Terahertz Compatible Absorber Based on Multilayer Film. *Front. Physics* **2021**, *9*, No. 633971.

(51) Wang, L.; Zheng, Z. H.; Gou, Y. C.; Liang, W. W.; Yu, W. Fabry-Perot Resonance Assisted Dual-Layer Coating with Enhanced Wavelength-Selective Reflection and Emission for Daytime Radiative Cooling. *Opt. Commun.* **2021**, *483*, No. 126673.